

Photonic Crystal Enhanced Microscopy on a 2D Photonic Crystal Surface

Weinan Liu, Siyan Li, Edmond Chow, Seemesh Bhaskar, Ying Fang, and Brian T. Cunningham*

Digital-resolution biosensing based on resonant reflection from photonic crystals (PC) has demonstrated significant potential for detection of proteomic and genomic biomarkers in serology, infectious disease diagnostics, and cancer diagnostics. An important intrinsic characteristic of resonant metamaterial surfaces is that enhanced electromagnetic fields are not uniformly distributed, resulting in spatially variable light-matter interactions with nanoparticle tags that signal the presence of biomarker molecules. In this work, the spatial uniformity of resonantly enhanced, surface-confined electromagnetic fields of a 1D PC is compared with a 2D PC with fourfold symmetry. When illuminated with unpolarized light, the simultaneously excited electromagnetic fields of transverse electric and transverse magnetic modes of the 2D PC present equally strong but complementary spatial distribution, leading to a >100% increased average near-field intensity accompanied with a >50% compressed standard deviation compared to the 1D PC. Utilizing Photonic Resonator Absorption Microscopy (PRAM) to experimentally measure the absorption uniformity of ≈ 80 nm gold nanoparticles distributed upon the PC surface, a >100% improvement of the signal uniformity is observed when using the 2D PC. Overall, improvement in AuNP detection contrast, uniformity, and point spread function is demonstrated by PRAM performed upon a 2D PC surface.

ultrasensitive approach for applications in life science research and disease diagnostics.^[1] Conventional biosensing techniques, such as surface plasmon resonance (SPR) refractive index biosensing have been widely used in medical diagnostics and environmental monitoring.^[2] These methods are cost-effective, efficiently robust, and able to provide label-free detection. However, for applications requiring extremely low detection limits, for example, single-molecule sensitivity, conventional methods are ineffectual. Compared to conventional biosensing methods, where the generation of a detectable signal requires gathering large numbers of target molecules to a transducer, digital resolution detection utilizes imaging-based or cytometry-based sensing platforms to count the detected analytes via enzymatic amplification reactions within small-volume droplets or through detection of nanoparticle tags that emit, absorb, or scatter light.^[3] Common methods such as

1. Introduction

Digital-resolution detection of genomic and proteomic biomolecules has emerged as a quantitatively accurate and

droplet digital polymerase chain reaction (ddPCR)^[4] and the Simoa technology attain high sensitivity while requiring droplet partitioning of the sample, thermal cycles (for ddPCR), and enzymatic amplification, representing complex workflows.^[5] Recent

W. Liu, S. Bhaskar, B. T. Cunningham
Department of Electrical and Computer Engineering
University of Illinois at Urbana-Champaign
306 N Wright St MC 702, Urbana, IL 61801, USA
E-mail: bcunning@illinois.edu

W. Liu, E. Chow, B. T. Cunningham
Holonyak Micro and Nanotechnology Laboratory
University of Illinois at Urbana-Champaign
208 N Wright St, Urbana, IL 61801, USA

S. Li, Y. Fang
Department of Pathobiology
University of Illinois at Urbana-Champaign
2001 S Lincoln Ave, Urbana, IL 61802, USA
S. Bhaskar, B. T. Cunningham
Carl R. Woese Institute for Genomic Biology
University of Illinois at Urbana-Champaign
1206 W Gregory Dr, Urbana, IL 61801, USA

B. T. Cunningham
Department of Bioengineering
University of Illinois at Urbana-Champaign
1406 W Green St, Urbana, IL 61801, USA

B. T. Cunningham
Department of Chemistry
University of Illinois at Urbana-Champaign
505 S Mathews Ave, Urbana, IL 61801, USA

B. T. Cunningham
Cancer Center at Illinois
University of Illinois at Urbana-Champaign
405 N Mathews Ave, Urbana, IL 61801, USA

 The ORCID identification number(s) for the author(s) of this article can be found under <https://doi.org/10.1002/admt.202401837>

© 2025 The Author(s). Advanced Materials Technologies published by Wiley-VCH GmbH. This is an open access article under the terms of the [Creative Commons Attribution](#) License, which permits use, distribution and reproduction in any medium, provided the original work is properly cited.

DOI: 10.1002/admt.202401837

innovations in microscopy techniques and nanoparticle contrast agents help overcome these challenges, showing enhanced capabilities for detecting analytes at lower detection limits. Fluorescence microscopy techniques, combined with bright fluorescent nanoparticle tags such as quantum dots and plasmonic fluors^[6] can also provide digital resolution detection of biomolecules, where photonic metamaterial surfaces, such as photonic crystals (PC), can enhance excitation, photon collection efficiency, and lifetime to provide enhanced nanoparticle detection contrast while using simple, inexpensive, and compact detection instruments.^[7]

Employing the strong light-matter interaction of nanophotonic structures in the context of biosensor microscopy has been demonstrated using SPR imaging microscopy,^[8] localized SPR imaging on an array of plasmonic nanorods,^[9] plasmonic metal thin film-based biosensing of significantly enhanced fluorescence,^[7a,b,10] photonic resonator enhanced interferometric scattering,^[11] and absorption microscopy.^[3,12] By enhancing the field intensity close to the analyte through exciting resonant electromagnetic (EM) modes, the detected signal (in terms of fluorescent emission photon output, absorption efficiency, or scattered photon output) can be increased by orders of magnitude. However, when improved sensitivity is induced by the enhanced near field, the high quality-factor, localized resonant modes always possess a non-uniform distribution of spatially localized EM hotspots, resulting in a position-dependent signal intensity. This intrinsic issue leads to a broad signal distribution and low detection accuracy where the image processing algorithm must be precisely tuned to select a signal-screening threshold that differentiates signals from background noise.^[11a] In other words, nonuniform EM field distribution can result in some nanoparticle reporters “hiding” in locations with low EM field, while the nanoparticles fortunate to land in the EM hotspots are detected with maximal contrast. Inevitably, when nanoparticles are randomly distributed across a metamaterial surface, there will be a resulting contrast distribution due to the continuum of spatially nonuniform EM field intensities.

In earlier reports, we introduced Photonic Resonator Absorption Microscopy (PRAM), which employs gold nanoparticle (AuNP) tags with localized surface plasmon resonance (LSPR) wavelengths that match the guided mode resonant reflection wavelength of a PC surface. In PRAM, hybrid coupling between the AuNP's LSPR resonance and the PC's guided mode resonance is used to enhance optical absorption for each surface-attached AuNP,^[13] leading to a localized reduction in reflected intensity, easily measured by illuminating the PC with a low-intensity LED and capturing the back-reflected light with an image sensor. While the initial PRAM used line scanning and spectral imaging, requiring ≈ 30 s to collect each image, we developed a more cost-effective and portable version (portable-PRAM, p-PRAM) by eliminating the spectrometer and capturing whole-frame images.^[12a,b,14] An upgraded automated portable PRAM (ap-PRAM) was recently introduced, featuring a motorized translation stage, autofocus, and temporal image collection, facilitating rapid automatic biomarker detection, extended field-of-view tiling, and single-molecule kinetic analysis.^[3] While the portable versions use scientific-quality steel precision-machined optical components with a desktop-sized footprint, we recently described an inexpensive and portable version (PRAM-mini) optimized

for point-of-care (POC) environments. In the PRAM-mini we replaced the metal-based precise optical fixtures with an inexpensive acrylic sheet as the breadboard, and utilized 3D-printed plastic fixtures to hold the less expensive optical components to produce a textbook-size instrument with a component cost of $\approx \$1000$.^[12c] Using PRAM-based detection, several digital resolution biomolecular assays were developed that utilize AuNP tags for detection of miRNA, antigens, and antibodies.^[15] It is possible to accelerate assays by utilize magnetic-plasmonic nanoparticle tags to overcome diffusion limitations.^[16] Overall, PRAM-based assays using AuNP tags provide sensitive digital-resolution detection of biomolecular targets without the need for sample partitioning into microdroplets or enzymatic amplification, resulting in simple (1-2 step) assay workflows and <30 min to provide a result.

In this work, we present a 2D fourfold symmetric PC consisting of ultraviolet (UV)-curable, square-hole epoxy arrays sputtered with a Titanium dioxide (TiO_2) layer and cured on a glass substrate. Due to the symmetry, the 2D PC is able to provide polarization-independent response and when it is illuminated with dual polarizations (TE + TM) at the resonant wavelength, the near field magnitudes of both TE and TM resonant modes will be efficiently enhanced to identical intensity but spatially aligned to orthogonal directions. Therefore, the distribution of TE and TM modes presents a complimentary profile. In areas where the near field is weak for the TE mode, the TM-polarized field is strong and vice versa, creating a uniform enhancement of the total near field. Numerical simulations of gold nanoparticle (AuNP) absorption cross section for 50 randomly distributed positions on the PC show that the signal's standard deviation (measure of error) of PRAM is reduced by 32% compared to the 1D PC counterpart. In PRAM, interfacing the plasmonic AuNPs by a biomolecular interaction pull-down mechanism assists in generation of the hotspots between the plasmonic AuNPs and the dielectric PC substrate. The resonant coupling at the interface results in reduced reflection intensity at the location of the surface-attached AuNPs, enabling digital counting of the captured molecules. We fabricated the 2D PC using a cost-effective replica molding method and experimentally measured polarization-independent reflection with the sample. Finally, we demonstrate enhanced image contrast (150%), signal robustness, and improved point spread function ($2/3$ smaller in size) than the 1D PC counterpart. Our work demonstrates more accurate, reliable, and high contrast detection of AuNPs for PRAM-based assays when performed upon a 2D PC surface.

2. Results and Discussion

2.1. Uniform Near-Field Enhancement of a 2D PC

The 2D PC consists of UV-curable epoxy 2D square-hole arrays that are replica molded and coated with TiO_2 , cured onto a glass substrate, as illustrated in **Figure 1a**. The period, duty cycle, hole depth, and TiO_2 thickness are designed to provide a high efficiency resonant reflection at a wavelength close to 625 nm (see the design strategy in **Figure S1**, Supporting Information). **Figure 1e** shows a schematic illustration of the 1D PC, for which the structural and material information has been previously reported.^[12a] By approximating the grating to a pure slab

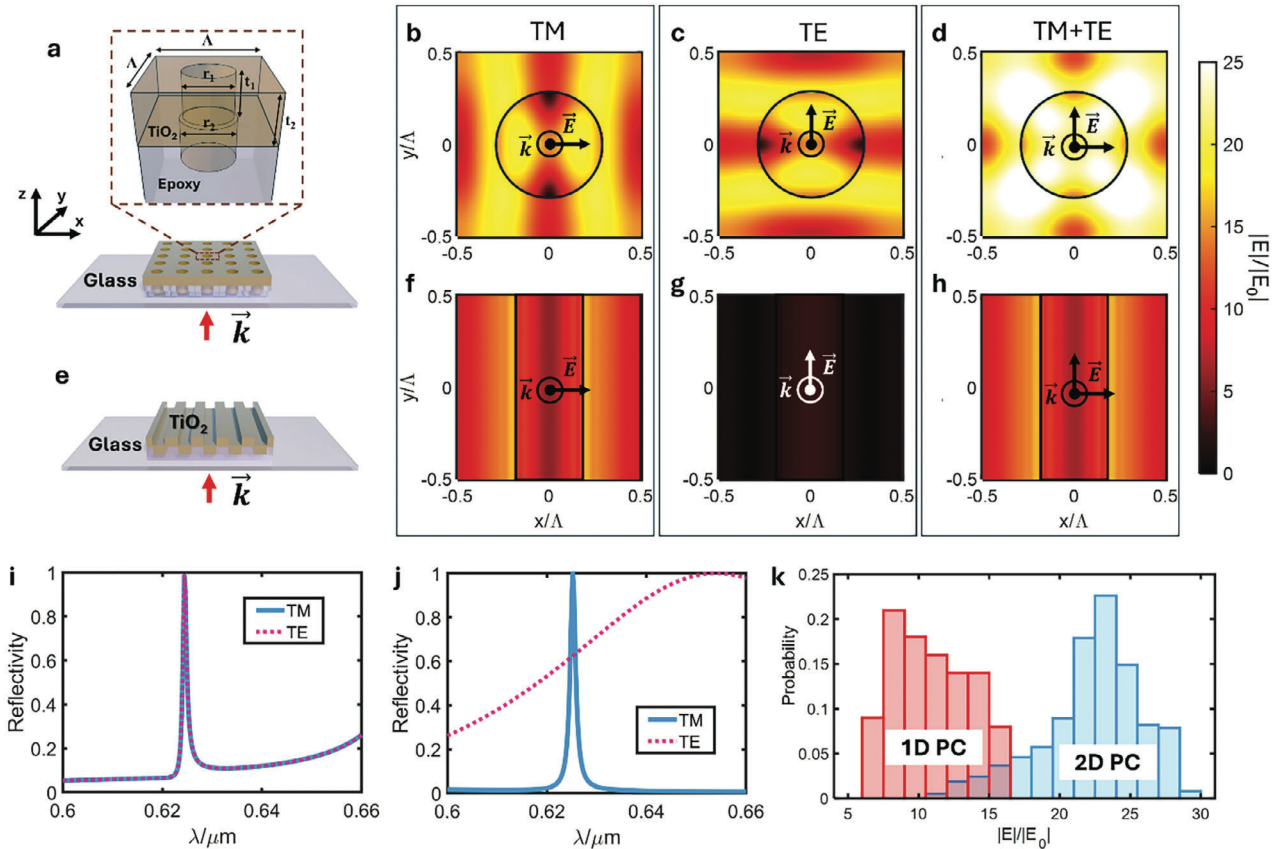


Figure 1. Uniform near-field enhancement by polarization-independent 2D photonic crystal (PC). a) Schematic illustration of the 2D PC. The structure is a nanopatterned UV-curable epoxy layer coated with high-index Titanium dioxide (TiO₂) and cured on a glass substrate. The design parameters include the period $\Lambda = 396$ nm, radius of inner and outer holes: $r_1 = 0.3 \Lambda$ and $r_2 = 0.325 \Lambda$, hole depth: $t_1 = 80$ nm, coating thickness: $t_2 = 95$ nm. Light is incident from below. b–d) Simulated near-field enhancement on the top of the 2D PC for transverse magnetic (TM), transverse electric (TE), and TM + TE hybrid polarizations at resonant wavelength. The xz -plane is defined as the plane of incidence hence the electric field is aligned with the x -axis for TM polarization. e) Schematic of the 1D PC. Corresponding geometric parameters can be found in ref. [12a] f,g) Sampled near-field enhancement on the top of the 1D PC for TM, TE, and TM + TE hybrid polarizations at resonant wavelength. i,j) Numerically calculated reflectivity of 2D and 1D PCs respectively for TM and TE polarizations from 600 to 660 nm. The TM and TE spectra of 2D PC are completely overlapped and they both present a resonant peak at 624.5 nm for 2D PC, whereas only the TM-polarized spectra of 1D PC shows a resonant peak at 625 nm. k) Statistical histogram of the surface-sampled near-field enhancement. The blue bars represent the data from the 2D PC (mean: 16.76 V m⁻¹, standard deviation (STD): 2.70 V m⁻¹) while the red bars represent the data from the 1D PC (mean: 8.24 V m⁻¹, STD: 2.04 V m⁻¹).

waveguide, the equation describing the coupling between a slab waveguide with a diffraction grating can be expressed as:^[17]

$$\begin{cases} \tan(\kappa_{i,r}d) = \frac{\kappa_{i,r}(\gamma_{i,r} + \delta_{i,r})}{\kappa_{i,r}^2 - \gamma_{i,r}\delta_{i,r}}, & (TE) \\ \tan(\kappa_{i,r}d) = \frac{n_w^2 \kappa_{i,r} (n_w^2 \gamma_{i,r} + n_w^2 \delta_{i,r})}{n_w^2 n_e^2 \kappa_{i,r}^2 - n_w^2 \gamma_{i,r} \delta_{i,r}}, & (TM) \end{cases} \quad (1)$$

where

$$\begin{cases} \kappa_{i,r} = \sqrt{n_i^2 k^2 - \beta_{i,r}^2} \\ \gamma_{i,r} = \sqrt{\beta_{i,r}^2 - n_w^2 k^2} \\ \delta_{i,r} = \sqrt{\beta_{i,r}^2 - n_e^2 k^2} \\ \beta_{i,x} = k \left(n_w \sin \theta_x - m \frac{\lambda}{\Lambda_x} \right), \quad \beta_{i,y} = k \left(n_w \sin \theta_y - n \frac{\lambda}{\Lambda_y} \right) \\ k = \frac{2\pi}{\lambda} \end{cases} \quad (2)$$

$i = 1, 2, 3, \dots$ is the mode order, $r = x, y$ indicates the x or y component, m, n are the grating diffraction order along x, y -axes, λ is the wavelength, θ_r is the incident angle along r -axis, Λ is the grating period, d is the waveguide thickness, n_w, n_e, n_i are the refractive index of the water, TiO₂, epoxy, respectively. By solving Equations (1) and (2) we can get the resonance wavelength λ for certain waveguide thickness d . For 1D PC, only x component needs to be calculated (no periodicity along y direction). Under normal incidence, the transverse propagation constant β_r becomes zero ($\theta_r = 0, \beta_r \geq 0$), hence Equation (1) for 1D and 2D PCs share the same formula. This observation inspired us to use geometric parameters similar to 1D PC to design a 2D PC resonates at 625 nm. The resonant near field of the PC (Figure 1b–d,f–h) is investigated by sampling the electric field (30 000 equally distributed sampling points) on the top surface of the TiO₂ layer, and the field distribution is numerically calculated by the rigorous coupled-wave analysis (RCWA) software S4.^[18]

Figure 1b–d shows the sampled electric field (total field, $|\vec{E}| = \sqrt{E_x^2 + E_y^2 + E_z^2}$, same as below) under TM, TE, and TM + TE (circular or 45-degree linearly polarized, simulated under the condition where the phase difference between TM and TE polarization is 90 degrees and 0 degrees, respectively) polarized normal incidence of 2D PC, respectively; Figure 1f–h indicates the sampled electric field of corresponding illumination for the 1D PC. A global color bar is used to allow direct comparison of the electric field distributions across different scenarios, where the uniform near-field enhancement can be clearly observed from the TM + TE hybrid illuminated 2D PC. Sampled electric fields with individual color bars are available in the Supporting Information (Figure S3, Supporting Information). The plane of incidence is defined as the xz -plane, hence the TM-polarized light has its electric field vector oriented along the x -axis, and TE-polarized light oriented along the y -axis. We observe that both PC designs present efficient near-field enhancement ($|\vec{E}|/|\vec{E}_0| \gg 1$, where \vec{E}_0 is the incident electric field) at the on-resonant illumination condition. The 2D PC demonstrates an identical-shape mode profile near the surface for both TE- and TM-polarizations except the TE mode is the 90-degree rotated version of TM mode, which is due to the 2D PC's four-fold symmetric structure. Note that for TE polarization, there is no near-field enhancement for the 1D PC because the resonant condition is not satisfied. One notable observation is that when both PCs are illuminated with TM + TE hybrid incidence, since TE and TM modes are orthogonal, the total field distribution is the superimposition of both TE and TM mode profiles. Thus, the near-field enhancement of the 2D PC is intensified and shows a uniform distribution since the weak-field areas emerging in Figure 1b,c are added by the strong field component of the orthogonal polarization. The near-field enhancement for the hybrid-illuminated 1D PC, however, exhibits an intensity close to that of TM illumination due to weak excitation of TE modes. The similarities of TM mode profile for the 1D and 2D PCs are investigated in Figure S2 (Supporting Information).

The reflection spectra for normal incidence of the 2D and 1D PCs are calculated by RCWA, as shown in Figure 11,j, respectively. The reflection spectra indicate the presence of asymmetric Fano resonance due to the coupling between the guided modes and the free-space propagating modes scattered off the PCs. Notice that the resonance quality factor for the 2D PC ($Q = 631$) is higher than that for the 1D PC ($Q = 431$), so in the 2D PC the interaction between the discrete guided modes and the continuum propagating modes becomes more prominent, enhancing the asymmetry associated with the Fano effect (Figure 1i).^[19] The polarization-independent reflection spectrum of the 2D PC enables resonance excitation with any polarization. In contrast, the 1D PC only permits resonance induction at a wavelength of 625 nm with TM-polarized light. Note that the full width at the half maximum (FWHM) of the spectrum of the 2D PC is designed to match that of the 1D PC. The statistical histogram of the sampled electric-field enhancement of TM + TE hybrid illumination on the TiO₂ surface is shown in Figure 1k. The average near-field enhancement factor ($|\vec{E}|/|\vec{E}_0|$) is observed to increase from 8.24 to 16.76, representing an improvement of 103%. The relative standard deviation,

STD_r , is used as the factor to evaluate the uniformity of the data:

$$STD_r(E) = STD(E)/Mean(E) \quad (3)$$

where the $STD(E)$ and the $Mean(E)$ are the standard deviation and the average of the sampled electric field, respectively, and smaller STD_r indicates better uniformity. The calculated $STD_r(E)$ for the 1D PC is 0.25, whereas for the 2D PC the value is 0.16. Compared to the 1D PC, the 2D design demonstrates a 56% improvement of the near-field uniformity.

2.2. 50-Point Measurement of AuNP Absorption Cross Section

PRAM is a digital resolution biosensing technique, which enables direct observation of single AuNPs by intensifying their absorption cross section σ_{abs}

$$\sigma_{abs} = 1/I_0 \iiint QdV \quad (4)$$

where I_0 is the incident intensity, Q is the power loss density in the AuNP, and the integral is taken over its volume. This boost of σ_{abs} is achieved by spectrally aligning the LSPR of the AuNP with the resonant reflection wavelength of the PC. Upon illumination under appropriate resonant conditions, the excited modes in the PC couple with the LSPR of surface-linked plasmonic AuNPs generating intense dielectric-metal hotspots.

Here, we present a finite element method (FEM) simulation (COMSOL Multiphysics)^[20] of the AuNP's absorption cross section (hybrid illumination for 2D PC and TM-polarized illumination for 1D PC), where we placed a AuNP at 50 randomly chosen locations on the surface of the PCs to compare the uniformity of the PRAM signal they provide by calculating the relative standard deviation of σ_{abs} , as shown in Figure 2. Figure 2a,b shows the top view of the unit cell of the 1D and 2D PCs, respectively. The red dots indicate the positions of the single AuNP placed at random (x,y) locations in the simulation, selected by the random number generator function of MATLAB. Since the AuNP occupies space, there are certain areas that the AuNP (red dot) cannot appear – such as regions where the distance to the wall is less than 40 nm within the groove/hole, shown as the shaded region inside the groove/hole of the two PCs. A two-step simulation was implemented where we first computed a background field from the plane wave incident on the PC, which we used to calculate the total field with the AuNP present. Figure 2c,d are the normalized histograms of the 50-point simulated σ_{abs} . The calculated relative standard deviation is 46.29% and 35.06% respectively, which demonstrates a 32% improvement of the uniformity for the 2D PC. The reduced enhancement of uniformity compared to the result of near-field calculation (56%) is reasonable since the AuNP is not an infinitely small point and the enhanced near field it couples with has a specific area, or represents an effectively averaged field, which leads to a marginal improvement in uniformity. As two representative samples, Figure 2e–h separately show the simulated total near field (after the second simulation step) and the spectral absorption cross section for 1D and 2D PCs for a AuNP placed in the center of the groove/hole.

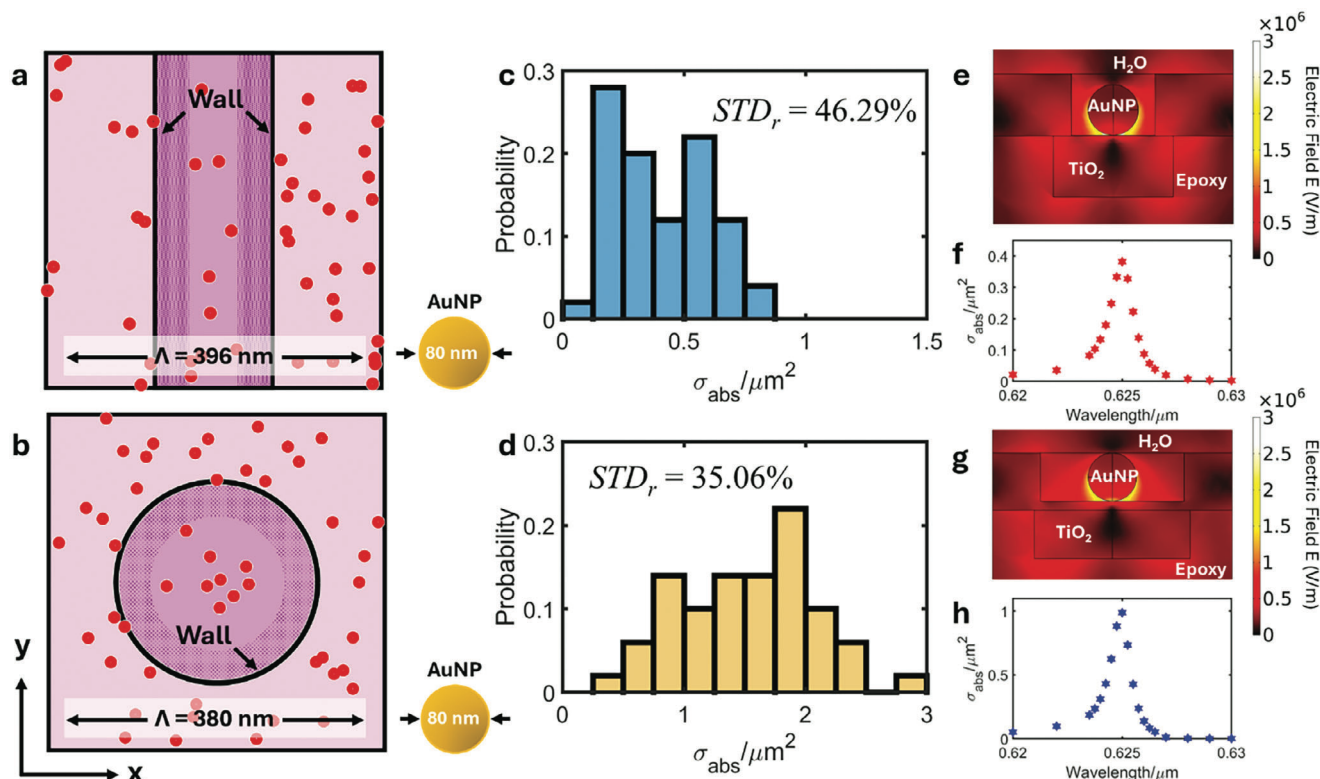


Figure 2. 50-point simulation for the uniformity enhancement of AuNP absorption. a,b) Top-view illustration of the unit cell for 1D (a) and 2D PC (b) (not to scale). The red dots are the positions of the AuNP set in the simulation software, whose coordinates were generated by a MATLAB script. c,d) Normalized histogram of the AuNP absorption cross section of 1D, 2D PC. The mean σ_{abs} is $0.82 \mu\text{m}^2$ and $1.52 \mu\text{m}^2$ and the standard deviation is $0.38 \mu\text{m}^2$ and $0.53 \mu\text{m}^2$ for 1D and 2D PC respectively. Therefore, the relative standard deviations (STD_r) are 46.29% and 36.06%. The simulation shows that the 2D PC demonstrates an 85% enhancement of the averaged σ_{abs} and a 32% of the uniformity over the 1D counterpart. For example Finite element method (FEM) simulation calculated total electric field within one unit cell of a AuNP presenting in the center of the groove/hole of the 1D/2D PC with normal incidence at the resonant wavelength. f,h) Spectral absorption cross section calculated by FEM simulation for the AuNP set in (e) and (g).

The line shape of the spectral σ_{abs} in Figure 2f,h shows a single peak at wavelength of 625 nm, where the EM near field is at its maximum.

2.3. Fabrication and Characterization

Numerous nano-fabrication techniques have been developed for PC fabrication including focused-ion beam (FIB) etching,^[21] direct UV laser writing,^[22] electron beam lithography (EBL),^[23] X-ray lithography.^[24] However, biosensing for POC detection applications must circumvent expensive and sophisticated fabrication devices, trained personnel, and long-turn processing, an efficient and cost-effective replica molding method is hence preferred for the 2D PC fabrication. There are two steps included in the replica molding: 1) a mold, which has an opposite profile to the structure we want to make is fabricated with a both physically and chemically robust material. We patterned the mold on a silicon substrate by EBL followed with inductive coupled plasma (ICP) etching of the silicon to generate the profile for the mold. 2) use the mold as a template to reproduce multiple nano-structure replicas in a polymer material. Figure 3a–e shows the step-by-step workflow of the replica molding method. A 5 μL UV-curable epoxy droplet was cast on the silicon mold (Figure 3a) and covered by a

coverslip (Figure 3b), followed by a 40 sec exposure under a 500 W UV lamp (Xenon RC-600, Figure 3c). The cured replica was gently lifted from the silicon mold (Figure 3d) and then deposited with a layer of TiO_2 (80-nm thickness) using a reactive radio frequency (RF) sputtering system (Kurt Lesker PVD 75, Figure 3e). Figure 3f,g are the scanning electron microscope (SEM) images of the EBL + ICP fabricated silicon mold. Figure 3h,i are the SEM images of the replica molded 2D PC. They all showed good consistency with our design, where the period and the filling factor were observed to be uniform across the patterned area. Characterization of the 2D PC via atomic force microscope (AFM) can be found in the (Figure S5, Supporting Information). Figure 3j shows a photo of the fabricated 2D PC.

The transmission spectrum of the PC was measured on a home-built optical setup, as shown in Figure 3k. The 2D PC was mounted on a rotation stage. Linearly polarized white light from a tungsten halogen lamp (Ocean Optics LS-1) collimated by two lenses (lens1: $f = 5 \text{ mm}$, lens 2: $f = 30 \text{ mm}$) was incident onto the PC surface (illumination area $\approx 25 \text{ mm}^2$). The zero-order transmitted light was collected by a fiber collimating lens and guided by an optical fiber into a spectrometer (Ocean Optics USB 2000). By rotating the polarizer, we measured the transmission spectra for both TE and TM polarization. Since the PC is comprised only of dielectric materials without loss, we simply use

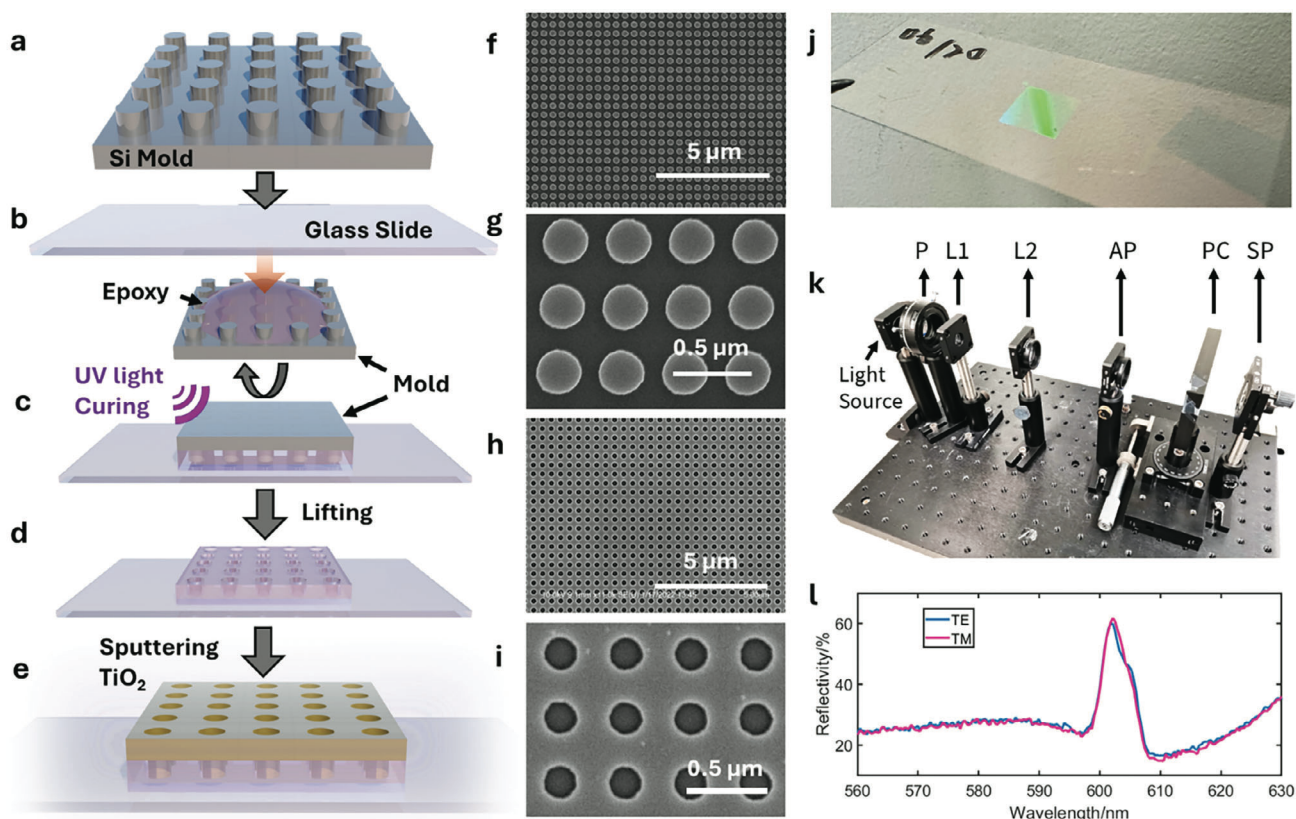


Figure 3. Cost-effective 2D PC fabrication and experimental setup of spectrum measurement. a) Silicon mold fabricated via a combination of electron beam lithography (EBL) and inductive coupled plasma (ICP) etching techniques. b) Placing a glass microscope slide over the epoxy drop-cast silicon mold. c) Ultraviolet (UV)-curing the epoxy to generate 2D hole array. d) Gently lifting the mold up. The cured epoxy is left on the glass slide. e) Sputtering an 80 nm thick TiO_2 layer on the sample by the reactive radio frequency sputtering system. f,g) Top view of the 11k- and 45k-fold magnified scanning electron microscope (SEM) images of the silicon mold. h,i) Top view of the 11k- and 45k-fold magnified SEM images of the 2D PC. j) 2D PC (the region reflecting green light) fabricated on a glass slide, holding on a tweezer. k) Homemade transmission optical setup to measure the spectrum of PC in air. P: polarizer. L1: lens 1. L2: lens 2. AP: aperture. PC: photonic crystal. SP: spectrometer. l) Measured reflectivity for TM- and TE-polarized light incident on the 2D PC sample.

$R = 100\% - T$ to calculate the reflectivity, where R is the reflectivity and T is the transmission. The measured reflectivity is shown in Figure 3l, where we observed a highly reflective peak and a good overlap of TE and TM polarizations, indicating the excitation of a polarization-independent resonance as expected for a fourfold symmetric PC nanostructure. Note the transmission measurement was performed with the PC surface exposed to air, thus the peak of the resonance is located near 602 nm. When the PC surface is covered with water, the peak wavelength shifts to 624 nm (Figure S6, Supporting Information).

2.4. PRAM-Based Detection of Surface-Captured AuNPs Using an Antibody-Antigen Binding Interaction

To compare the performance of the 1D and 2D PCs through capture and imaging of a moderately high density of immobilized AuNP tags and PRAM-based detection, we performed a pull-down assay based upon immobilization of an antigen on the PC biosensor to capture AuNPs prepared with immobilized

antibody. The approach used in this work is adapted from a blocking biosensor assay in a previous report^[25] using the ap-PRAM instrument^[26] (Figure S7, Supporting Information) for detection of SARS-CoV-2 antibody. Here, our goal is not to perform an assay, but rather to capture many AuNPs on the PC surface with biomolecular bonds, so we may compare the PRAM-imaged AuNP features when the assay is performed with 1D and 2D PCs. In a blocking biosensor assay, the SARS-CoV-2 N protein is first immobilized on the surface of 1D and 2D PCs as the target antigen. To block any remaining binding sites on the PC surface, the Power Block reagent (Thermo Fisher) is applied next. After a wash step to remove free blocking reagent, the test sample containing anti-SARS-CoV-2 antibodies is introduced into each sensing region, followed by incubation at 37 °C for 60 min with gentle agitation to maximize antigen-antibody binding efficiency. In the second step, a solution of monoclonal antibody (mAb)-conjugated AuNPs targeting the SARS-CoV-2 N protein is added to each reaction and incubated at room temperature for 15 min. The 15-min incubation time is optimized for distinguishing infected and uninfected serum samples obtained

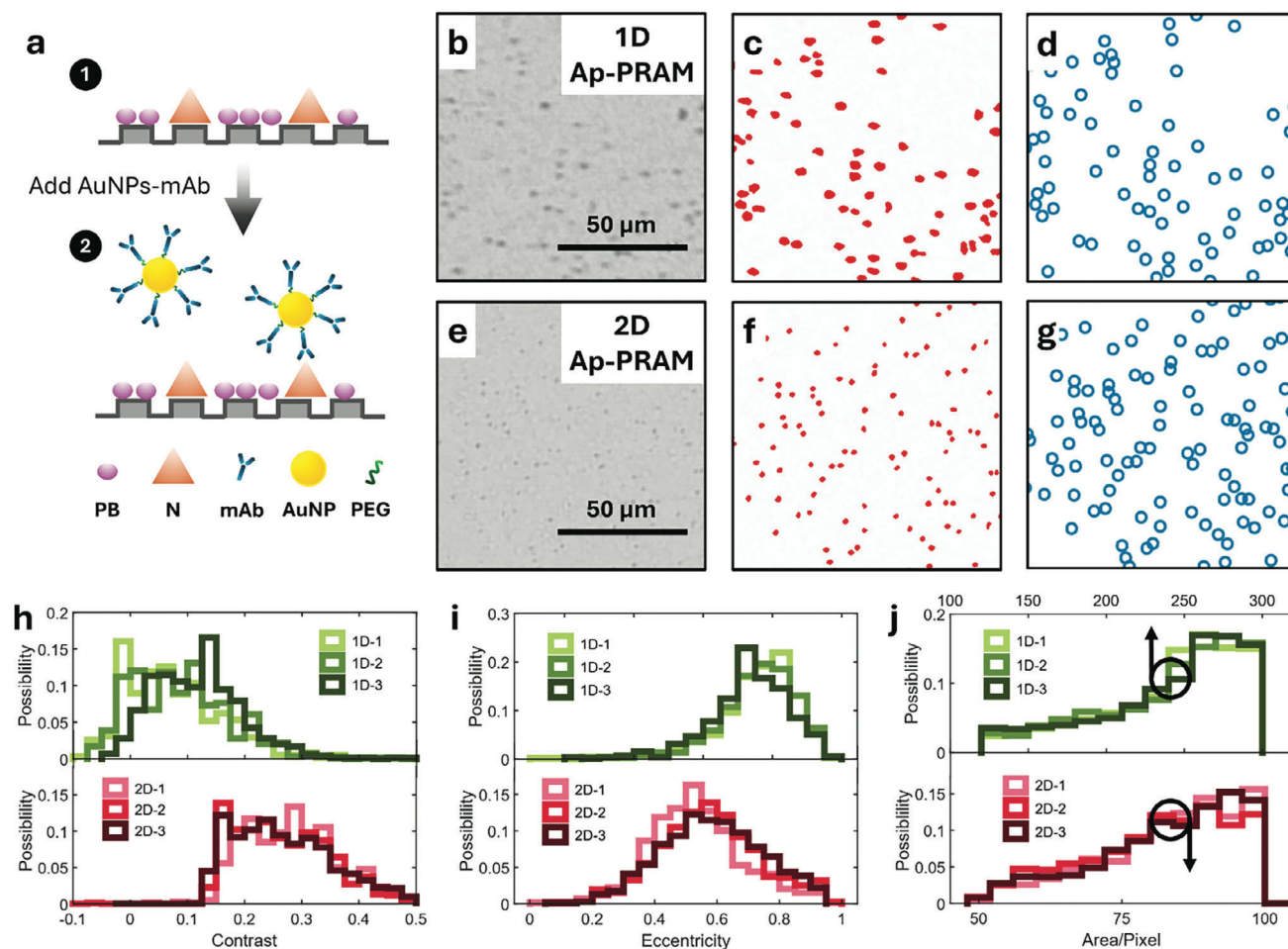


Figure 4. Performance of 1D versus 2D PC in the blocking assay for capture of antibody-linked AuNPs to an antigen-linked PC surface. a) Flowchart for the blocking assay. 1) Coating the SARS-CoV-2 nucleocapsid (N) protein and the Power Block on the PC surface. 2) Introducing AuNPs-PEG-mAb conjugates into the sensing area. The AuNP conjugate binds to the viral antigen proteins immobilized on the PC surface. PEG: Polyethylene Glycol. b,e) ap-PRAM images of the blocking assay. The images are processed by Tophat filtering to remove the uneven background for better visualization. The size of bound AuNP in 2D ap-PRAM is obviously smaller than they are in 1D ap-PRAM c,f) AuNP mask (red dots) recognized by our image processing algorithm. d,g) Digitalized representation of the counted AuNPs. These identical blue circles are centered at the centroid of each dark spot in the ap-PRAM image. h–j) Normalized histogram of the signal contrast, spot eccentricity, spot area, for the 1D and 2D ap-PRAM images, respectively.

from clinical cases. Extending the assay time beyond this point did not significantly enhance the detection limit and, instead, led to increased background signals that could hinder assay sensitivity and specificity. The mAb-conjugated AuNPs selectively bind only to N proteins on the PC surface that have not interacted with antibodies in the test sample, as binding sites on antigens occupied by test sample's antibodies prevent further interaction with the mAb-conjugated AuNPs. The blocking biosensor assay is considered as an “inverse” assay, in which greater concentration of the analyte results in fewer AuNPs attached to the biosensor surface at the conclusion of the assay protocol, and thus the greatest AuNP density is obtained for a negative sample that contains no analyte. We intentionally selected this type of assay for comparison of AuNP features in PRAM images between 1D and 2D PCs because a large number uniformly distributed AuNPs is ensured. Here, we perform the assay only in the negative control condition (with no antibody in the test sample) to ensure that many AuNPs are linked to the PC surface by antibody-antigen bonds.

The blocking biosensor assay incorporates anti-SARS-CoV-2 N mAb and purified SARS-CoV-2 N protein to detect species-nonspecific antibody generation across SARS-CoV-2 infected animals and human beings.^[27] Figure 4a shows a schematic illustration of the immunoassay. 1) the 1D and 2D PCs were coated with 10 μL of nucleocapsid (N) protein ($8 \mu\text{g mL}^{-1}$) and incubated overnight at 4 $^{\circ}\text{C}$. Following this, each sensing region received 20 μL of 1x Power Block (Thermo Fisher) and was incubated at 37 $^{\circ}\text{C}$ for 1 h to effectively minimize nonspecific binding of AuNPs during the assay. The PCs were then washed three times with 1x phosphate buffered saline with Tween (PBST). Polyethylene Glycol (PEG) was used to conjugate the AuNP and the mAb. To ensure homogeneity, the AuNPs-PEG-mAb conjugate was sonicated for 10 s and assessed for aggregate absence using dynamic light scattering (DLS). 2) The prepared PC is placed onto the sample-holding stage of the ap-PRAM instrument. The wash reagent was then removed using a pipette. Subsequently, 10 μL of AuNPs-PEG-mAb conjugates were introduced into the

sensing area. The reaction mixture was allowed to incubate for 15 min. Following this incubation, the PCs were illuminated at normal incidence by a red LED (M617F2, Thorlabs, center wavelength: 625 nm), and the reflected image of the PC was captured by the instrument's image sensor, where each AuNP on the PC was displayed as a location with lower intensity in the image. To optimize performance, the light incident on 1D and 2D PCs is TM and TE + TM hybrid polarized by rotating the polarizers' angle to 0 and 45 degree, respectively. This procedure was systematically repeated at three different locations on both 1D and 2D PCs, with each sample analyzed at least twice to ensure reliability and reproducibility of the results.

Figure 4b,e shows a representative region of one of the ap-PRAM images (field-of-view (FOV): 102 μm x 102 μm) of the assay using 1D and 2D PCs, respectively. Figure 4c,f separately show how the image processing algorithm produced mask of Figure 4b,e, which mark the pixels belonging to the dark spots generated by the AuNP binding. A digitized representation of the ap-PRAM images (Figure 4b,e) is shown in Figure 4d,g, where identical blue rings/circles are employed to replace the dark spots of the original ap-PRAM image and are placed at the centroid of each recognized mask to provide an abstract and concise visualization of the detected AuNPs. Details of the image processing algorithm can be found in the (Figure S8, Supporting Information).

To demonstrate the performance of the 1D and 2D PCs used in the assays, we developed an image processing algorithm to analyze the contrast, eccentricity, and area of the dark spots observed in the ap-PRAM images. First, the algorithm calculates the average pixel intensity within the detected mask of each AuNP spot I_i ($i = 1, 2, 3, \dots, n$, n is the number of detected AuNPs). Next, the algorithm uses a Tophat filter to produce the background with no AuNP present. The mean intensity of the background I_{bg} is calculated using all the pixels in the Tophat-filtered image. Then, the contrast of the i th spot is computed by $Contrast_i = I_i - I_{bg}$. The three-position contrast histogram of all the AuNP spots appearing in the ap-PRAM images of 1D and 2D PCs is shown in Figure 4h. The top panel reflects the contrast calculated with the 1D PC while the bottom represents the 2D PC's outcome. Due to the spatially nonuniform illumination from the LED (greatest intensity occurs in the center of the image) and the moderate contrast of 1D ap-PRAM image, there are some spots whose gray scale intensity is larger than the average of the background, resulting in instances of negative contrast in the 1D PC's contrast histogram. The Tophat algorithm is thus used to remove the uneven illumination background to improve the AuNP counting accuracy. For the 1D PC, the 1D-1, 2, 3 data include 580, 642, 707 counted AuNPs, while the 2D-1, 2, 3 data contain 589, 915, 1633 counted AuNPs, respectively. The histogram is normalized according to this number of AuNPs. To analyze the correlation of the three data sets, we calculated the Pearson correlation coefficient according to:

$$\rho(M, N) = \frac{1}{N-1} \sum_{i=1}^n \left(\frac{M_i - \mu_M}{\sigma_M} \right) \left(\frac{N_i - \mu_N}{\sigma_N} \right) \quad (5)$$

where μ_M and σ_M are the mean and standard deviation of M , respectively, and μ_N and σ_N are the mean and standard deviation of N . The calculated Pearson coefficient for the contrast correla-

tion between 1D-1 and 1D-2, 1D-2 and 1D-3, 1D-3 and 1D-1 are 0.84, 0.92, 0.87, and the Pearson coefficient for 2D-1 and 2D-2, 2D-2 and 2D-3, 2D-3 and 2D-1 are 0.86, 0.98, 0.84, respectively, which are all close to 1, demonstrating good reproducibility and repeatability. The measured contrast of the AuNP spots on 1D PC is: 0.12 ± 0.090 , on 2D PC is 0.30 ± 0.085 (normalized gray-scale range), indicating a 150% enhancement of signal contrast and a 165% improvement of contrast uniformity (comparing the STD_r : $\frac{0.090}{0.12} / \frac{0.085}{0.30} = 265\%$) for 2D over 1D PC. The 150% contrast boost is close to the calculated enhancement of the near field. However, the experimentally measured uniformity improvement is significantly greater than the simulation outcome. This is the result of the uneven background illumination and the weak near-field enhancing capability of 1D PC where some spots are observed to have negative contrast, which leads to a small mean contrast with the same order-of-magnitude standard deviation, resulting in a sizeable STD_r .

In addition to the characterization of the contrast, we also examined the eccentricity of the AuNP-generated dark spots from 1D and 2D ap-PRAM images. The eccentricity of every connected component (the detected mask of each AuNP spot) $E_i (i = 1, 2, 3, \dots, n)$ was extracted and plotted as a histogram shown in Figure 4i. The data sets present interesting correlations. The average of eccentricity for AuNPs in 1D PC is 0.72, while the average of 2D PC is 0.58, which means the spot obtained in 2D PC ap-PRAM has better roundness compared to the 1D PC. This is a specifically meaningful improvement for imaging-based biosensing since the image processing algorithm always requires some pre-knowledge of the signal to enumerate them, a higher standard of circularity enables the algorithm to screen out non-signal objects (artifacts, scratches and so on) that usually appear as a non-circular shape.

Finally, we compared the size of the AuNP-generated spots between the 1D and 2D ap-PRAM and plotted their normalized histogram in Figure 4j. Although the actual size of the AuNPs is ≈ 80 nm diameter in all cases, the observed dark spots in the PRAM images are determined by the point spread function (PSF) of the instrument, combined with the spatial characteristics of the PC reflected resonance quenching when the AuNP absorbs energy within the PC's evanescent field. It is evident that the size of the AuNP-generated features on the 2D PC are smaller compared to the 1D PC, as shown in Figure 4e. Note that the algorithm employs the upper and lower limit of the area (120–300 pixels for 2D, 50–100 pixels for 1D) as the cut-off size threshold to accurately recognize the AuNPs from other non-nanoparticle features, this is the reason why there are two steep boundaries in these histograms. The overall spatial extent of the detected AuNPs upon the 2D PC is 1/3 of the 1D PC. Since the diameter of the AuNPs are much smaller than the wavelength, the dark spots in ap-PRAM image represent their PSF. In microscopy theory, smaller PSF indicates that the blurriness surrounding the point is suppressed, resulting in enhanced resolution within the imaging system, corresponding to a sharper image. Therefore, utilizing the 2D PC, the PSF of AuNPs observed by PRAM are substantially refined. Though the limit of detection (LoD) of 2D PC-based blocking assays will not be drastically improved by a finer PSF because the LoD is mainly affected by the noise coming from nonspecific binding, we anticipate that the elevated AuNP imaging resolution will assist in more accurate AuNP binding

Table 1. Comparison of SARS-CoV-2 detection techniques.

Refs.	Biosensor	Biomarker	Digital-resolution	Assay duration
Ref. [30]	2D PC	SARS-CoV-2 spike protein	No	<15 min
Ref. [31]	1D PC	anti-SARS CoV-2 antibodies	No	10 min
Ref. [32]	2D PC	SARS-CoV-2 spike protein	No	N/A (computational study)
Ref. [33]	Digital FLISA ^{a)}	Nucleocapsid protein	Yes	>60 min
Ref. [34]	Indirect ELISA ^{b)}	IgG, IgM, and IgA antibodies	No	>75 min
Blocking Assay	2D PC surface (this work)	SARS-CoV-2 mAb	Yes	15 min

^{a)} FLISA: Fluorescence-linked immunosorbent assay; ^{b)} ELISA: Enzyme linked immunosorbent assay.

reporting (enhanced selectivity) to enable differentiation of samples with similar concentrations, or to reduce the time needed for detection. **Table 1** shows the comparison of the blocking assay used in this work with other similar SARS-CoV-2 protein detection techniques.

3. Conclusion and Outlook

We designed, fabricated, and characterized a fourfold symmetric 2D PC to serve as a substrate surface for detection of AuNPs by PRAM. When the device is illuminated by TE + TM-hybrid polarization, the excited dual-resonant EM modes create a uniformly enhanced near-field profile, significantly improving the consistency of the light-matter interaction across the surface-exposed positions upon which AuNPs are randomly distributed during PRAM-based digital resolution biosensing assays. Numerical simulation and experimental detection show that utilizing the 2D PC within the PRAM biosensing instrument provides a substantial enhancement to the uniformity, signal-to-background intensity (contrast) and PSF compared to the uniaxial 1D PC counterpart. Further, the 2D PC was fabricated by an efficient and cost-effective replica molding technique, enabling high-throughput and inexpensive manufacturing for POC detection scenarios. 3D PC is able to provide even more design degree of freedom, however, in terms of POC biosensing features such as compactness, weight, fabrication difficulty and cost, surface photonic devices (1D and 2D PCs) currently demonstrate more advantages over the 3D PC.

Digital resolution biosensing is a rising technology that is highly promising for next-generation healthcare monitoring. Current challenges about digital resolution biosensing include excessive manufacturing cost and complex biosensing mechanisms induced inferior robustness and accuracy. In a previous report,^[12c] we demonstrated a miniature, low-cost (\approx \$500 USD) version of the PRAM instrument and the cost for each assay was \approx \$2.5 USD. With significant performance enhancement, we expect that the 2D PC can improve the robustness and accuracy of digital resolution biosensing assays that use AuNPs as tags for individual biomolecules, detected with the compact and inexpensive PRAM instrument. In addition, the presented 2D PC can be an ideal substrate for surface-enhanced Raman spectroscopy (SERS) and surface plasmon-coupled emission (SPCE)/photonic crystal-coupled emission (PCCE) applications.^[28]

Further, it is important to elaborate on the highlight of this work from the perspective of metasurface design and applica-

tion. The hole arrays in our structure that comprise the 2D PC, when integrated with plasmonic antennas, help concentrate the electromagnetic (EM) fields into the nanoregimes between the PC and the plasmonic nanoantennas, in the so-called “hotspots”, thereby significantly improving sensitivity. While the nanoparticle-on-a-mirror (NPoM) configuration has been studied for several decades, they predominantly rely on the plasmonic NPs over the plasmonic thin films. On account of the lossy nature of the plasmonic substrates, the PCs have been widely used in sensor development. Moreover, the PCs render the possibility to tune the resonant wavelength to the desired region of the visible spectrum vis-à-vis nearly fixed plasma frequency of plasmonic substrates. Recently, metallo-dielectric hybrid interfaces are gaining importance on account of their ability to generate intense field confinement and enhancement as compared to metal-metal or dielectric-dielectric counterparts. Moreover, the periodicity and arrangement of the holes in 2D PCs of the underlying all-dielectric PC present the quintessential field distribution, while the precise positioning of the plasmonic antennas over the hole arrays enables deterministic, position-dependent sensing. This approach provides control over the localized field enhancement, improving the resolution and sensitivity of the sensor proposed in this work. We believe that the ability to tune sensor responses by adjusting the antenna positions offers a novel approach for highly sensitive, position-dependent detection, which is valuable for applications in chemical and biosensing. Overall, we envision this approach to be suitable for simple, rapid, and sensitive assays for a variety of biomolecular target analytes using inexpensively manufactured sensors and instruments.

4. Experimental Section

Fabrication of the Photonic Crystal Mold: Electron beam lithography (EBL) was used to pattern the mold template on a silicon wafer. The detailed fabrication procedure is as follows: The silicon (Si) template, featuring an 8×8 mm² array composed of 260 nm diameter disks with a pitch of 396 nm, was fabricated via a combination of EBL and inductive coupled plasma (ICP) etching techniques. Initially, a 200 nm layer of maN2410 negative EBL resist was spun onto a silicon substrate. Subsequently, exposure was carried out utilizing a 20 nA beam current with the Elionix 150 kV EBL system (ELS-G150), employing a single pixel exposure strategy with a defocused beam at a dose of $9\,000\,000 \mu\text{C cm}^{-2}$ to expedite the exposure process. Following exposure, the Si template underwent development in ma-D532 developer for 90 s, followed by a 2-min rinse in deionized (DI) water. The maN2410 resist layer (200 nm) served as the etching mask for the subsequent ICP etching step, facilitating the etching of 80 nm of

silicon. The etching process utilizes SF₆ and CHF₃ gases at a pressure of 5 mT with 600 W ICP power. Post-etching: the silicon template underwent cleaning in NMP solution at 80 °C for 30 min, followed by a brief O₂ plasma descum process to remove any residual maN resist.

AFM Analysis: All AFM data was collected using an Asylum Research MFP-3D AFM instrument, and the analysis was performed using freely available Gwyddion software. The median of differences flattening was adopted.

Preparation and Functionalization of the PC: The process begins by immersing the PC in a glass jar filled with acetone and sonicating it for 2 min. This step is repeated with isopropyl alcohol (IPA) and Milli-Q water for thorough cleaning. The PC is then dried under a nitrogen stream and placed in a 60 °C oven to remove any residual moisture. Surface activation is performed using an oxygen plasma generator at 100% power for 10 min. A 5% solution of 3-Aminopropyltriethoxysilane (APTES, Sigma-Aldrich) is prepared by mixing 47.5 mL of tetrahydrofuran (THF, Sigma-Aldrich) with 2.5 mL of APTES. The activated PC is then immersed in this APTES solution and incubated for 1 h on a shaker at 600 rpm and room temperature. After incubation, the APTES solution is discarded, and the PC is cleaned again using THF, acetone, ethanol, and Milli-Q water in a sonication process. Finally, the PC is dried, wrapped in aluminum foil to shield it from light, and stored in a desiccator for up to one month, ensuring it is prepared for future functionalization and assays.

Preparation of Antigen and Monoclonal Antibody: The N antigen was produced and purified following the methods outlined in our previous study.^[27a] The purified protein was dialyzed in 1x phosphate-buffered saline (PBS) at 4 °C and subsequently concentrated using polyethylene glycol 8000 (Thermo Fisher Scientific, Waltham, MA). The SARS-CoV-2 N protein-specific monoclonal antibody #127-3 was also developed in our prior research.^[29]

Synthesis of Spiky Core–Shell AuNP: A two-step growth method is used for synthesizing the spiky core-shell gold nanoparticles (AuNPs). 25 µL of a commercially available 20 nm nanoparticle seed solution (Cytodiagnosics, 3 M) was first incubated in 600 µL of a 20 mM sodium citrate solution for 30 min with moderate shaking. Following this, the nanoparticles were washed three times by centrifugation at 20 000 g and then redispersed in 2 mL of a 6 mM sodium citrate solution (Sigma-Aldrich). Next, 4 mL of a 0.5 mM HAuCl solution (Sigma-Aldrich) was brought to a boil, and 2 mL of the nanoparticle seed solution was quickly added while stirring vigorously at 700 rpm. The mixture reacted for 10 min at boiling temperature, during which the solution changed color from brown to burgundy. Deionized water was added as needed to maintain a consistent volume. The solution was then cooled while stirring for an additional 10 min, followed by three rounds of centrifugation at 4000 g. The resulting smooth spherical core-shell AuNPs were resuspended in 1.5 mL of a 2 mM sodium citrate solution to serve as seeds for the next step. For the growth of the spiky gold coating, a mixture was prepared with 5 mL of 0.25 mM HAuCl, 65 µL of the NP seeds (absorbance at 535 nm = 3.0), and 11 µL of 1% (w/v) sodium citrate, all stirred vigorously. Next, 500 µL of a 30 mM hydroquinone solution (Sigma-Aldrich) was quickly injected to initiate the reaction. The growth solution was allowed to react for 30 min at room temperature while stirring consistently at 700 rpm, during which the solution transitioned from pink to blue. The resulting spiky AuNP solution was washed three times at 1000 g and resuspended in a 0.1% (w/v) Pluronic F-127 solution for long-term storage.

Anti-N mAb–AuNP Conjugation: First, a fresh aliquot of SH-PEG-NHS (MW 5000, JenKem Technology, Plano, TX, USA) is diluted in Milli-Q water to a final concentration of 4 µM. Next, 20 µg of the anti-SARS-CoV-2 N mAb is gently mixed with the SH-PEG-NHS solution at room temperature, using a pipette to ensure thorough mixing without vigorous agitation. This mixture is then incubated on a shaker at 900 rpm for 2 h to facilitate the conjugation of SH-PEG to the mAb. After conjugation, the mixture is filtered using a MilliporeSigma Amicon Ultra-0.3 Centrifugal Filter Unit to remove any unbound PEG, performed at 4 °C to maintain the integrity of the proteins and linker. The concentrated SH-PEG-mAb conjugate is recovered and quickly combined with AuNPs in a non-stick microcentrifuge tube, avoiding vortexing to protect the delicate conjugates. The AuNPs and SH-PEG-mAb are incubated overnight at 4 °C to promote efficient binding

of the mAb to the AuNPs. Following incubation, the conjugates undergo DLS analysis to confirm an increase in particle size, indicating successful conjugation. The solution is then stabilized by adding filtered 2% BSA and incubated further to ensure complete coating of the conjugates. Excess mAbs are removed by centrifugation at 1000 rcf for 5 min, and the conjugates are resuspended in a 10% PBST (Pierce) solution for final storage at 4 °C, where they remain stable for up to one week.

Statistical Analysis: The statistical analysis of experimental data was performed by using Matlab (version R2021b, MathWorks, Natick, MA, USA). Continuous variables are expressed as mean ± STD, (sample size $n = 30\,000$ for the surface electric field, $n = 50$ for the 50-point AuNP absorption simulation, $n = 580, 642, 707$ for the AuNP count with 1D PC, $n = 589, 915, 1633$ for the AuNP count with 2D PC).

Supporting Information

Supporting Information is available from the Wiley Online Library or from the author.

Acknowledgements

The authors gratefully acknowledge funding from the National Institutes of Health (No. R01 EB026805, No. R01AI166791), the National Science Foundation (CBET 22-32681), and the USDA AFRI Nanotechnology grant (AG NIFA 2024-67021-42825). S.B. was supported by IGB postdoctoral fellowship from the Carl R. Woese Institute for Genomic Biology. W.L. thanks the research scientists Elbashir Araud, Dr. Nantao Li, Skye Shepherd, Joseph Tibbs, Priyash Barya, for their support. The support from the Asylum Research MFP-3D AFM; Hitachi S-4800 High Resolution SEM; Au-Pd Sputter Coater – Emscope SC 500; the associated staff and research scientists at clean room facility and BioNanotechnology Laboratory (BNL) at Holonyak Micro & Nanotechnology Lab (HM-NTL) and Materials Research Laboratory is gratefully acknowledged. The authors express their genuine gratitude toward the feedback provided by all the members of the Nanosensors group, HMNTL, during scientific discussions.

Conflict of Interest

Brian T. Cunningham is a co-founder of Atzeo Biosensors, which has a license agreement with the University of Illinois for intellectual property associated with PRAM.

Data Availability Statement

The data that support the findings of this study are available from the corresponding author upon reasonable request.

Keywords

Digital Resolution Biosensors, Near-field, Photonic Crystals, Surface Plasmons

Received: October 31, 2024

Revised: December 19, 2024

Published online:

[1] Q. Huang, N. Li, H. Zhang, C. Che, F. Sun, Y. Xiong, T. D. Canady, B. T. Cunningham, *Lab Chip* **2020**, *20*, 2816.

- [2] M. Piliarik, H. Vaisocherová, J. Homola, in *Biosensors and Biodetection*, (Eds: A. Rasooly, K. E. Herald), Humana Press, Totowa, NJ **2009**.
- [3] W. Liu, T. Ayupova, W. Wang, S. Shepherd, X. Wang, L. D. Akin, M. Kohli, U. Demirci, B. T. Cunningham, *Biosens. Bioelectron.* **2024**, *264*, 116643.
- [4] a) J. Jin, S. Vaud, A. M. Zhelkovsky, J. Posfai, L. A. McReynolds, *Nucleic Acids Res.* **2016**, *44*, e116; b) H. Tian, Y. Sun, C. Liu, X. Duan, W. Tang, Z. Li, *Anal. Chem.* **2016**, *88*, 11384.
- [5] a) L. Cohen, M. R. Hartman, A. Amardey-Wellington, D. R. Walt, *Nucleic Acids Res.* **2017**, *45*, e137; b) L. D. Smith, Y. Liu, M. U. Zahid, T. D. Canady, L. Wang, M. Kohli, B. T. Cunningham, A. M. Smith, *ACS Nano* **2020**, *14*, 2324.
- [6] a) J. Luan, A. Seth, R. Gupta, Z. Wang, P. Rathi, S. Cao, H. Gholami Derami, R. Tang, B. Xu, S. Achilefu, J. J. Morrissey, S. Singamaneni, *Nat. Biomed. Eng.* **2020**, *4*, 518; b) R. Gupta, P. Gupta, S. Wang, A. Melnykov, Q. Jiang, A. Seth, Z. Wang, J. J. Morrissey, I. George, S. Gandra, P. Sinha, G. A. Storch, B. A. Parikh, G. M. Genin, S. Singamaneni, *Nat. Biomed. Eng.* **2023**, *7*, 1556.
- [7] a) P. Barya, Y. Xiong, S. Shepherd, R. Gupta, L. D. Akin, J. Tibbs, H. Lee, S. Singamaneni, B. T. Cunningham, *Small* **2023**, *19*, 2207239; b) Y. Xiong, Q. Huang, T. D. Canady, P. Barya, S. Liu, O. H. Arogundade, C. M. Race, C. Che, X. Wang, L. Zhou, X. Wang, M. Kohli, A. M. Smith, B. T. Cunningham, *Nat. Commun.* **2022**, *13*, 4647; c) Y. Zhuo, B. T. Cunningham, *Sensors* **2015**, *15*, 21613; d) L. L. Chan, S. Gosangari, K. Watkin, B. T. Cunningham, *Apoptosis* **2007**, *12*, 1061; e) L. L. Chan, S. Gosangari, K. Watkin, B. T. Cunningham, *Sensors and Actuators B* **2008**, *132*, 418; f) P. C. Mathias, N. Ganesh, L. L. Chan, B. T. Cunningham, *Appl. Opt.* **2007**, *26*, 2351; g) S. M. Kim, W. Zhang, B. T. Cunningham, *Opt. Express* **2010**, *18*, 4300; h) R. D. Peterson, W. L. Chen, B. T. Cunningham, J. E. Andrade, *Biosens. Bioelectron.* **2015**, *74*, 815; i) S. George, V. Chaudhery, M. Lu, M. Takagi, N. Amro, A. Pokhriyal, Y. F. Tan, P. Ferreira, B. T. Cunningham, *Lab Chip* **2013**, *13*, 4053; j) H. Y. Wu, B. T. Cunningham, *Nanoscale* **2014**, *6*, 5162; k) W. Zhang, N. Ganesh, P. C. Mathias, B. T. Cunningham, *Small* **2008**, *4*, 2199; l) V. Chaudhery, M. Lu, C. S. Huang, J. Polans, R. Tan, R. C. Zangar, B. T. Cunningham, *Opt. Lett.* **2012**, *37*, 2565.
- [8] a) S. Wang, X. Shan, U. Patel, X. Huang, J. Lu, J. Li, N. Tao, *Proc. Natl. Acad. Sci. USA* **2010**, *107*, 16028; b) A. M. Maley, G. J. Lu, M. G. Shapiro, R. M. Corn, *ACS Nano* **2017**, *11*, 7447; c) H. Yu, X. Shan, S. Wang, N. Tao, *Anal. Chem.* **2017**, *89*, 2704.
- [9] S. Chen, M. Svedendahl, T. J. Antosiewicz, M. Käll, *ACS Nano* **2013**, *7*, 8824.
- [10] a) S.-H. Cao, W.-P. Cai, Q. Liu, Y.-Q. Li, *Annu. Rev. Anal. Chem.* **2012**, *5*, 317; b) M. Chen, S.-H. Cao, Y.-Q. Li, *Anal. Bioanal. Chem.* **2020**, *412*, 6085; c) V. S. K. Cheerla, K. M. Ganesh, S. Bhaskar, S. S. Ramamurthy, S. C. Neelakantan, *Langmuir* **2023**, *39*, 7939.
- [11] a) N. Li, T. D. Canady, Q. Huang, X. Wang, G. A. Fried, B. T. Cunningham, *Nat. Commun.* **2021**, *12*, 1744; b) L. Liu, J. Tibbs, N. Li, A. Bacon, S. Shepherd, H. Lee, N. Chauhan, U. Demirci, X. Wang, B. T. Cunningham, *Biosens. Bioelectron.* **2023**, *228*, 115197.
- [12] a) T. D. Canady, N. Li, L. D. Smith, Y. Lu, M. Kohli, A. M. Smith, B. T. Cunningham, *Proc. Natl. Acad. Sci. USA* **2019**, *116*, 19362; b) S. Ghosh, N. Li, Y. Xiong, Y.-G. Ju, M. P. Rathslag, E. G. Onal, E. Falkiewicz, M. Kohli, B. T. Cunningham, *Biomed. Opt. Express* **2021**, *12*, 4637; c) K. Khemtonglang, W. Liu, H. Lee, W. Wang, S. Li, Z. Y. Li, S. Shepherd, Y. Yang, D. G. Diel, Y. Fang, B. T. Cunningham, *Biomed. Opt. Express* **2024**, *15*, 5691.
- [13] Q. Huang, B. T. Cunningham, *Nano Lett.* **2019**, *19*, 5297;
- [14] a) Y. Zhuo, L. Tian, W. Chen, H. Yu, S. Singamaneni, B. T. Cunningham, presented at 2014 36th Annual Int. Conf. IEEE Engineering in Medicine and Biology Society, August **2014**; b) Y. Zhuo, H. Hu, W. Chen, M. Lu, L. Tian, H. Yu, K. D. Long, E. Chow, W. P. King, S. Singamaneni, B. T. Cunningham, *Analyst* **2014**, *139*, 1007;
- [15] a) X. Wang, S. Shepherd, N. Li, C. Che, T. Song, Y. Xiong, I. R. Palm, B. Zhao, M. Kohli, U. Demirci, Y. Lu, B. T. Cunningham, *Angew. Chem., Int. Ed.* **2023**, *62*, 202217932; b) T. D. Canady, N. Li, L. D. Smith, Y. Lu, M. Kohli, A. M. Smith, B. T. Cunningham, *Proc. Natl. Acad. Sci.* **2019**, *116*, 19362; c) B. Zhao, C. Che, W. Wang, N. Li, B. T. Cunningham, *Talanta* **2021**, *225*, 122004; d) B. Zhao, W. Wang, N. Li, T. Garcia-Lezana, C. Che, X. Wang, B. Losic, A. Villanueva, B. T. Cunningham, *Talanta* **2022**, *241*, 123256; e) C. Che, N. Li, K. D. Long, M. A. Aguirre, T. D. Canady, Q. Huang, U. Demirci, B. T. Cunningham, *Lab Chip* **2019**, *19*, 3943.
- [16] C. Che, R. Xue, N. Li, P. Gupta, X. Wang, B. Zhao, S. Singamaneni, S. Nie, B. T. Cunningham, *ACS Nano* **2022**, *16*, 2345.
- [17] G. Quaranta, G. Basset, O. J. F. Martin, B. Gallinet, *Laser Photonics Rev.* **2018**, *12*, 1800017.
- [18] V. Liu, S. Fan, *Comput. Phys. Commun.* **2012**, *183*, 2233.
- [19] M. F. Limonov, M. V. Rybin, A. N. Poddubny, Y. S. Kivshar, *Nat. Photonics* **2017**, *11*, 543.
- [20] COMSOL Multiphysics. v. 6. 3. www.comsol.com. COMSOL AB, Stockholm, Sweden.
- [21] Y. K. Kim, A. J. Danner, J. J. Raftery, K. D. Choquette, *IEEE J. Sel. Top. Quantum Electron.* **2005**, *11*, 1292.
- [22] J.-H. Klein-Wiele, P. Simon, *Opt. Express* **2013**, *21*, 626.
- [23] P. J. Bock, P. Cheben, J. H. Schmid, J. Lapointe, A. Delâge, S. Janz, G. C. Aers, D.-X. Xu, A. Densmore, T. J. Hall, *Opt. Express* **2010**, *18*, 20251.
- [24] C. Luo, Y. Li, S. Susumu, *Opt. Laser Technol.* **2012**, *44*, 1649.
- [25] S. Li, W. Wang, W. Liu, C. Chen, S. Shephard, F. Yuan, J. M. Reinhart, D. Diel, B. T. Cunningham, Y. Fang, bioRxiv **2024**, 2024.06.21.600129.
- [26] W. Liu, T. Ayupova, W. Wang, S. Shepherd, X. Wang, L. D. Akin, M. Kohli, U. Demirci, B. T. Cunningham, *Biosens. Bioelectron.* **2024**, *264*, 116643.
- [27] a) H. Ferrin Neal, Y. Fang, R. Johnson Craig, P. Murtaugh Michael, D. Polson Dale, M. Torremorell, L. Gramer Marie, A. Nelson Eric, *Clin. Vaccine Immunol.* **2004**, *11*, 503; b) F. Yuan, V. Petrovan, L. G. Gimenez-Lirola, J. J. Zimmerman, R. R. Rowland, Y. Fang, *Pathogens* **2021**, *10*, 760.
- [28] a) B. Rai, R. Malmberg, V. Srinivasan, K. M. Ganesh, N. S. V. Kambhampati, A. Andar, G. Rao, C. B. Sanjeevi, K. Venkatesan, S. S. Ramamurthy, *ACS Sens.* **2021**, *6*, 4360; b) S. Bhaskar, A. K. Singh, P. Das, P. Jana, S. Kanvah, S. Bhaktha B N, S. S. Ramamurthy, *ACS Appl. Mater. Interfaces* **2020**, *12*, 34323; c) S. Bhaskar, W. Liu, J. Tibbs, B. T. Cunningham, *Appl. Phys. Lett.* **2024**, *124*, 161102; d) B. Rai, D. Suter, V. Srinivasan, K. Venkatesan, S. S. Ramamurthy, *J. Phys. Chem. C* **2021**, *125*, 16681; e) R. Javaid, N. Sayyadi, K. Mylvaganam, K. Venkatesan, Y. Wang, A. Rodger, *J. Raman Spectrosc.* **2020**, *51*, 2408.
- [29] F. Yuan, C. Chen, M. Covaleda Lina, M. Martins, M. Reinhart Jennifer, R. Sullivan Drew, G. Diel Diego, Y. Fang, *mSphere* **2023**, *8*, e00067.
- [30] D. Kawasaki, H. Yamada, K. Sueyoshi, H. Hisamoto, T. Endo, *Biosensors*, *12*, 200.
- [31] A. Occhicone, A. Sinibaldi, D. Chiappetta, P. Di Matteo, T. Pileri, N. Danz, F. Sonntag, P. Munzert, M. Allegretti, V. De Pascale, C. Mandoj, F. Michelotti, *Biosens. Bioelectron.: X* **2023**, *15*, 100413.
- [32] H. Miyani, R. Agrahari, S. K. Gowre, P. K. Jain, M. Mahto, *Meas. Sci. Technol.* **2023**, *34*, 074004.
- [33] X. Dou, Z. Zhang, B. Liu, C. Li, Y. Du, F. Tian, *Anal. Bioanal. Chem.* **2023**, *415*, 6155.
- [34] S. Luo, J. Xu, C. Y. Cho, S. Zhu, K. C. Whittaker, X. Wang, J. Feng, M. Wang, S. Xie, J. Fang, A. S. Huang, X. Song, R.-P. Huang, *Laborat. Med.* **2022**, *53*, 225.